IIETA International Information and Engineering Technology Association
Advancing the World of Information and Engineering

Annales de Chimie - Science des Matériaux
Vol. 48, No. 4, August, 2024, pp. 539-549
Journal homepage: http://iieta.org/journals/acsm

Influence of WC Content on Microstructure of WC-Ni Coatings on AISI 18-2Mn Austenitic Stainless Steel Using TIG Cladding

Abdul Sameea Jasim Jilabi*, Aws Ali Oleiwi

Faculty of Materials Engineering, University of Babylon, Hillah 51002, Iraq

Corresponding Author Email: sameeakilabi@gmail.com

https://doi.org/10.18280/acsm.480411

Received: 11 June 2024
Revised: 1 August 2024
Accepted: 13 August 2024
Available online: 30 August 2024

Keywords:
tungsten inert gas (TIG) cladding, Ni/WC composite coatings, AISI 18-2Mn austenitic stainless steel

ABSTRACT

At present, the use of tungsten inert gas (TIG) cladding is an effective method for surface modification of steel-based alloys. This work aims to investigate the effect of tungsten carbide-nickel (WC-Ni) composite coatings deposited using TIG cladding on the surface properties of AISI 18-2Mn austenitic stainless steel substrates. Additionally, the study focuses on considering the influence of WC mass percentage in WC-Ni coatings on these properties. 1mm thick pre-placed WC-Ni composite pastes with different wt.% of WC (35, 50, 65, 80 and 95) were used to deposit the coating layers applying a travel speed of 67 mm/min and a current value of 130A. Optical microscopy and scanning electron microscopy exhibited various microstructures across the clad layers, mostly WC particles scattered throughout the matrix and nickel solid solution dendrites. The cooling rates and the WC density within the composite will determine, the dendrites were little or dense, equiaxial or columnar, finer or coarser, and more or less densely branched. Rather than in the dendrites, the matrix was the main location of the Fe element that was transferred from the substrate material to the molten pool, as demonstrated by energy dispersive spectroscopy, whereas the distribution of the W element clearly indicated the locations and orientations of the dendrites.

1. INTRODUCTION

The distinctive and demanding qualities of stainless steel make them valuable alloys. Their significance is demonstrated by the range of applications they can be used for, from straightforward ones like furniture and kitchenware to incredibly intricate ones like spacecraft and construction. Thicker and more robust constructions are now possible due to their resilience to corrosion and long-term use. In addition to being robust, hygienic, adaptable, and recyclable, they also come in a large range of shape, color, and form choices [1, 2].

Stainless steels consist of three main microstructure types: ferritic, austenitic, and martensitic. Stainless steels fall into multiple classes based on these three main microstructures. These stainless steels are precipitation-hardening, duplex, austenitic, martensitic and ferritic [1]. Based on the chemical composition, each material's mechanical, chemical, and physical characteristics change, but they are all distinguished by their capacity to form a protective oxide layer that heals itself, preventing corrosion and enhancing corrosion and oxidation resistance through increased chromium content [3]. For example, with respect to these different characteristics, fully austenitic stainless steels are non-magnetic, whereas martensitic and ferritic alternatives are ferromagnetic [1].

NITRONIC 32, also referred to as nitrogen-strengthened austenitic stainless steel, is an iron-based AISI 18-2Mn alloy that is primarily composed of manganese and chromium.

To obtain particular qualities, varying amounts of silicon, nickel, molybdenum, niobium, vanadium, and/or molybdenum are also added. With strong elevated-temperature strengths, low magnetic permeability, excellent cryogenic properties, and roughly twice the yield strength of Type 304, NITRONIC 32 is a great choice [4].

Recently, the scientific community has come to understand that surface modification is required because new materials typically have insufficient surface qualities for wettability, adhesion, corrosion resistance, or even drag reduction. Finding an alloy with a surface behavior distinct from the bulk is also challenging for a number of reasons. Increased mechanical and fatigue resistance, improved thermal stability, and increased resistance to corrosion and wear (for being in either a high or low temperature), Many factors, such as magnetic, electrical, or specific optic or light exposure behavior, have led to surface modification. It is also necessary for oleophobicity, hydrophobicity, biocompatibility, (bio) fouling, and even their combined effects. To achieve and improve these properties in metals and alloys, one must either apply a surface modification strategy based on direct action on the metal, create a coating that offers these properties, or functionalize its surface for complex requirements [5].

There are two types of surface modification: chemical and physical. Physical modification, such as etching, grit-blasting, and machining, alters the surface's topography or morphology while causing little to no change in chemistry. Atomic layer deposition, electrochemical deposition, and plasma and chemical vapor deposition are examples of well-established

chemical processes. Chemical treatment can produce single layer coatings or coatings with multiple layers of varying compositions, ion infusion, surface oxidizing, nitriding, or carbiding [6]. Despite Laser cladding has a wide range of applications in various industries due to its notable ability to produce coatings with dense microstructure and strong metallurgical bonding with substrates. Nonetheless, the TIG technique was selected for use in this paper due to its broad applicability, ease of transportation, and accessibility for a variety of materials. It also features a high deposition rate, a low dilution ratio, and cheap equipment costs. Furthermore, both automated and manual processes can be used [7, 8].

2. METHODOLOGY

AISI 18-2Mn stainless steel plates with dimensions of 10*70 mm were used for this experiment. In accordance with the American Iron and Steel Institute (AISI), the austenitic stainless steel plates' chemical composition, which served as the study's substrates [4] is displayed in Table 1. The raw material was used to create the pieces (substrates) to be coated, with each piece measuring 100 mm in length. The chemical composition of the raw material was examined using the OXFORD instrument at the Al-Razi Metallurgical Research Center in Tehran, Iran, based on RMRC-WI-560-112-04. The chemical composition of the raw material used as a substrate is displayed in Table 1 (average of three readings). This composition complies with nominal AISI 18-2Mn Nitronic 32.

2.1 Cladding materials

2.1.1 Pure nickel powder

According to ASTM E 1621-21, the chemical composition analysis of Table 2 at the Al-Razi Metallurgical Research Center in Tehran, Iran, using XRF technology, showed that the purity of Ni powder was 99.64 weight percent. Utilizing a Bettersize 2000 laser particle size analyzer, which can be found in the Ceramic Engineering and Building Materials Department laboratories of the Faculty of Materials Engineering at the University of Babylon, the particle size of Ni powder was examined. The range of particle sizes was between 3.7 and 63.4 μm.

Table 1. Nominal and actual chemical composition of the substrate material

Alloy		Chemical composition (wt.%)								Spec. Symbol (AISI)
		C	Mn	Si	Cr	Ni	N	P	S	
A.S.S.	Nominal	0.15 max.	11.0-14.0	1.0 max.	16.5-19.0	0.5-2.5	0.2-0.45	0.045 max.	0.03 max.	18-2Mn
	Actual	0.065	10.45	0.43	13.5	1.2	0.18	0.044	0.005	(Nitronic 32)

Table 2. Chemical analysis of nickel powder

Element	Ni	Mg	Si
wt. %	99.64	0.2	0.16

2.1.2 Tungsten carbide powder

Using the Bettersize 2000 laser particle size analyzer, the WC powder's particle size was determined to be between 3 and 6 μm. According to ASTM E 1621-21, Table 3 displays the results of an XRF chemical composition analysis of WC powder performed at the Al-Razi Metallurgical Research Center. Based on the XRD result, stoichiometry was used to determine the weight percent of the C element in the XRF analysis.

Table 3. Chemical analysis of tungsten carbide powder

Element	W	C
wt. %	93.87	6.13

2.1.3 Binding material

The binder material for the pre-placed WC-Ni composite paste was polyvinyl alcohol (PVA). The PVA specifications according to ME Scientific Engineering Ltd., a German product packed in the UK, are displayed in Table 4.

Table 4. Polyvinyl Alcohol specifications

Product	PVA code	Molecular formula	Viscosity
MESE	8-88	$(C_4H_6O_2.C_2H_4O)_x$	8 mPa.s (in 4% aqu. Solution)

2.2 Preparatory steps for the cladding process

Before commencing the cladding process, the following processes have been meticulously completed:

(1) removing grease, oils, and other impurities from the substrate surfaces.

(2) Using a universal milling machine, eight slots measuring 1×6×30 mm were created in the substrates (Figure 1(a)) for the pre-placed WC-Ni composite coatings to be deposited.

(3) Using a magnetic stirrer found in the laboratories of the Metallurgical Engineering Department/Faculty of Materials Engineering/University of Babylon, 4.0% of PVA was dissolved in 96% of hot distilled water (50°C) for 15 minutes in order to prepare the binder.

(4) In the Metallurgical Engineering Department's laboratories, various weight percentages of WC powder (35, 50, 65, 80, and 95) and Ni powder were measured using a sensitive balance in order to create WC-Ni mixtures.

(5) These mixtures were mixed with a 4.0% PVA solution binder to create a pre-placed WC-Ni composite paste that would be later deposited in the slots, keeping the powder mixtures under the flow of Ar gas during TIG cladding (Figure 1(b)).

(6) drying the paste for one hour at 100°C in the oven.

The cladding procedure was completed using a TIG welding machine in conjunction with a lathe machine to create automatic and constant tungsten arc travel along the composite layers. The study examined the impact of varying WC powder weight percentages (35, 50, 65, 80, and 95) with Ni powder on the microstructure of the five coated clad layer samples. The TIG cladding parameters are shown in Table 5. The microstructure and topography of various areas on the prepared specimen surfaces were then visualized using an optical microscope by examining the cross-section of the clad layers. This inspection was carried out at the laboratories of Al-Razi Metallurgical Research Center-Tehran/Iran based on ASTM E883-2017. Microstructural examination and chemical

composition analysis were performed using SEM and EDS at the labs of Al-Razi Metallurgical Research Center-Tehran/Iran.

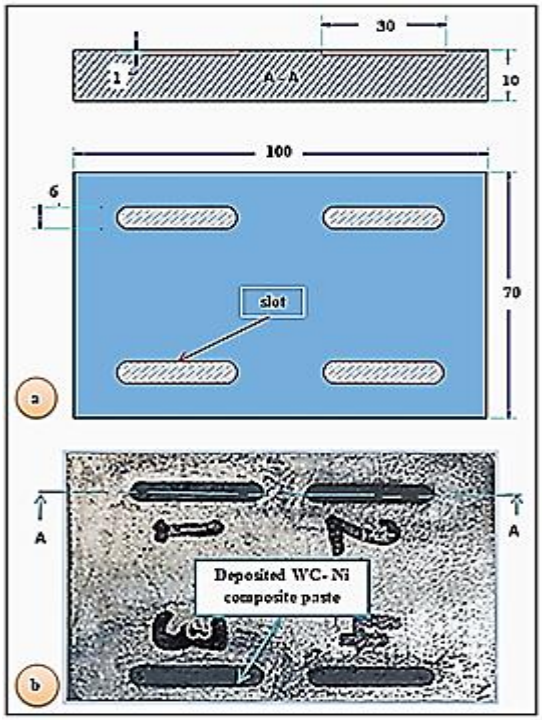

Figure 1. (a)-dimensions of slots machined in the substrates in mm, (b)-WC-Ni composite paste deposited in the slots

Table 5. TIG cladding parameters.

Cladding by the Use of	Pure WC Powder of (wt.%)				
	35	50	65	80	95
Clad symbol	**C1**	**C2**	**C3**	**C4**	**C5**
Travel speed (mm/min.)	67				
Current value (A)	130				
Voltage value (V)	15				
Position	Flat				
Polarity	DCEN				
Thickness of layer (mm)	1				
Ar gas flow rate (l/min)	10				
Ar gas purity (%)	99.999				
Arc length (mm)	3				
Tungsten electrode diameter (mm)	2.4				
Tungsten electrode type	Thoriated Tungsten ESAB-WT20				

3. RESULTS AND DISCUSSION

The experimental work was presented and its results discussed. Through the use of the EDS, the OM, SEM evaluated the microanalysis of MMC coatings applied to austenitic stainless steel substrates.

3.1 Micrography

Before discussing the microstructural variations across the coated samples, it is necessary to get acquainted with the microstructure of the substrate material prepared from AISI 18-2Mn austenitic stainless steel. OM and SEM show in Figure 2 that the microstructure of the substrate alloy was austenite grains noting the appearance of twinning. Table 1 shows the chemical composition of this having elevated levels of Mn (up to 10.45 weight percent) and N (up to 0.18 weight percent), which serve as some substitutes for Ni in the stabilization of austenite. This is the reason why austenite grains appear on microscopic examination [7]. Since N has more solubility than carbon in austenitic iron and is a stronger austenite stabilizer and solid solution strengthener without significantly reducing fracture toughness, it has advantageous properties [8].

According to studies [9-11], as the concentration of N increases, single and polycrystalline austenitic stainless steels exhibit a greater propensity to form planar dislocation structures. These structures lead to enhanced strain hardening through slip band formation and, in some cases, deformation twinning by reducing the material's ability to cross-slip [12]. Accordingly, Figure 2 makes twinning evident.

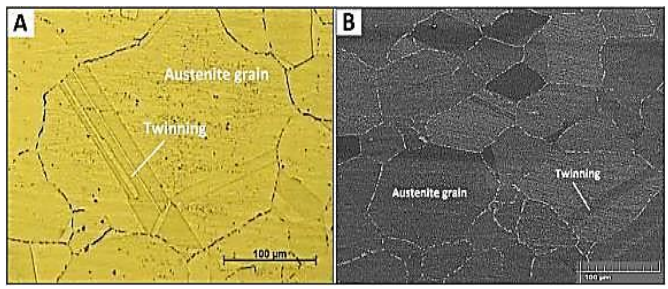

Figure 2. Microstructure of the substrate material using (A): OM and (B): SEM

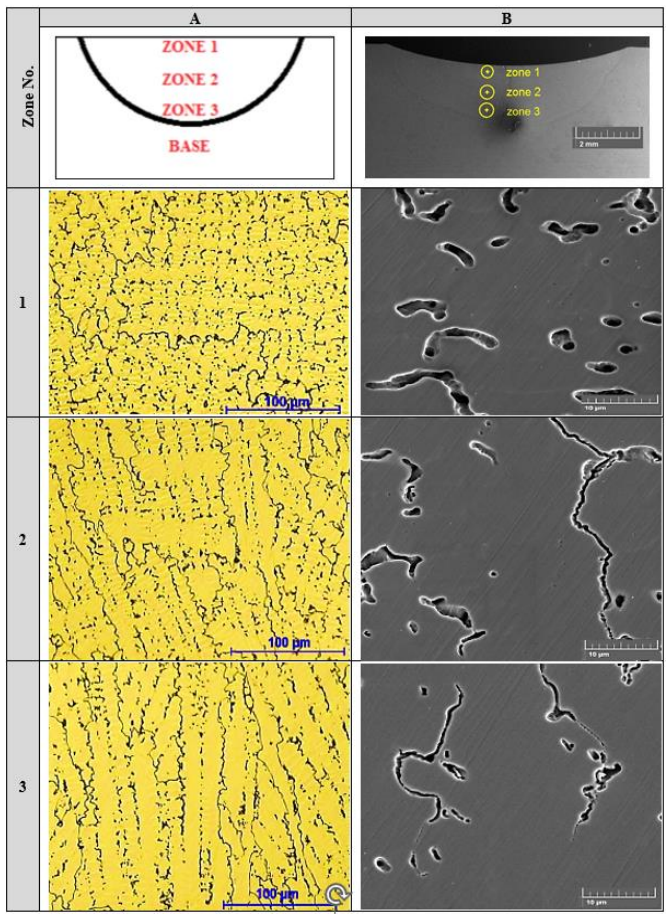

Figure 3. Microstructural map of the C1 sample at different depths along the centerline of the cross section of the clad layer using (A): OM and (B): SEM

The microstructures of the clad layer and surrounding substrate regions varied in each sample, as revealed by microscopy. The chemical compositions of the coating layers and the significant temperature gradients that the sample is subjected to, ranging from the melting point to the temperature of the heat-insensitive substrate, are the causes of these variations. This is usually followed by a rapid rate of cooling, primarily brought on by the atmosphere and the comparatively cold substrate.

Figure 3 shows microstructures of the C1 sample covered with a 35% WC-Ni composite by TIG cladding, with a current of 130 A and a travel speed of 67 mm/min. Along the centerline of the clad layer cross section, micrography was done for three zones at varying depths. Figure 3 exhibits that the optical microstructure of Zone 1 (near the clad surface) consists of nickel solid solution dendrites with insoluble intermetallic compounds of WC particles distributed through an austenitic matrix. Figure 4 shows the optical microstructure of this zone with higher magnifications.

The relatively slow travel speed (67 mm/min) of the TIG torch used with this clad sample introduced excessive heat input, which consequently caused the WC particles to partially dissolve and disperse into irregular shapes within the matrix. The presence of a relatively large amount of high melting point WC compounds in the molten pool (2720°C compared to that of Ni 1455°C) makes many incompletely dissolved WC particles remain in the solidification structure as reported in 2005 by Zhang et al. [13].

The WC granular structure solidifies as a nucleation particle in the molten pool first during the solidification process because of its higher melting point. A Ni solid solution dendrite structure, which has a lower melting point, gradually precipitates around it [14].

The gradually decreasing density of carbides with irregular shapes in Zone 2, where the carbides accumulated irregularly with a poor distribution near the clad surface, in addition to a small portion of them presented at the clad-substrate interface. Figure 5 shows the microstructure of Zone 2 with higher magnifications.

The microstructure of the clad layer's bottom region was displayed by the OM for Zone 3 in Figure 3, and Figure 6 provides a higher magnification of this zone's microstructure.

It should be emphasized that while columnar grains predominated in Zone 3, the OM for Zone 2 showed a mixture of equiaxed and columnar nickel solid solution grains (Figures 3A, 5 and 6). The columnar grains are oriented perpendicular to the cooling surface (clad-substrate interface) towards the clad surface. This is because heat typically flows from the molten pool towards the adjacent colder substrate metal.

The microstructure of the substrate next to the interface was composed of austenite grains, as predicted based on the chemical composition (Table 1). Due to the uncontrolled heating and the relatively high cooling rate resulting from the adjacent colder substrate metal, this region appeared to suffer from severe recrystallization, as shown in Figure 7. The EDS map along the centerline of the cross section of the C1 clad layer at various depths is shown in Figure 8.

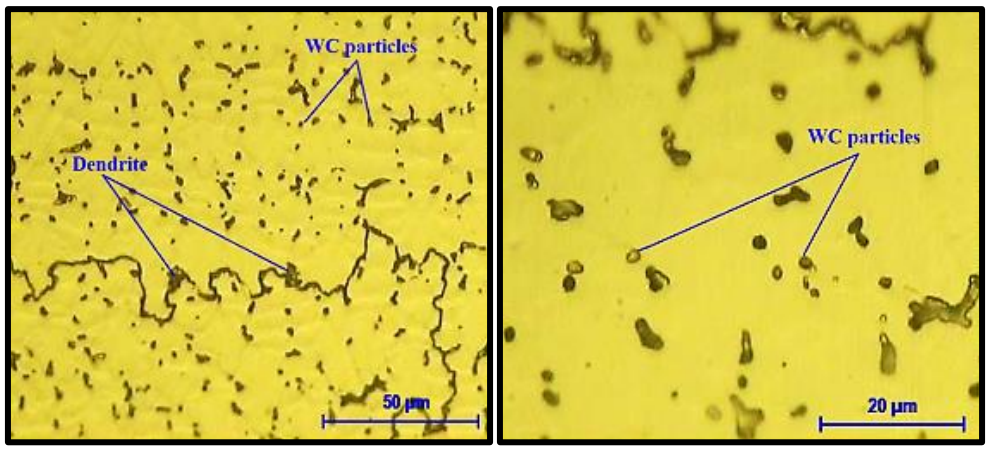

Figure 4. Optical microstructure of Zone 1 of C1 sample with higher magnifications

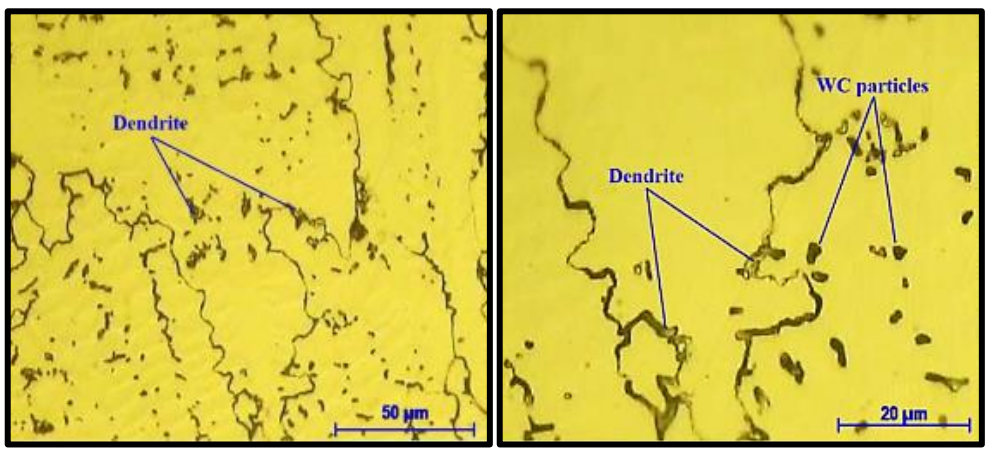

Figure 5. Optical microstructure of Zone 2 of C1 sample with higher magnifications.

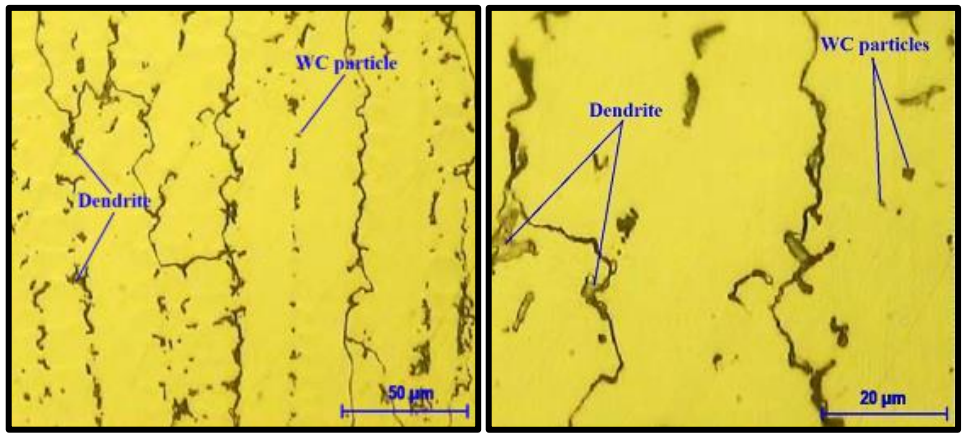

Figure 6. Optical microstructure of Zone 3 of C1 sample at higher magnifications

It is evident from the Figure 8 that iron at the three test points was predominant (59.9 wt.% on average) at the expense of other elements (12.5% Ni, 8.0% W, 8.6% Mn and 11.0% Cr by weight on average), although the preplaced composite paste of this sample consisted of 65 wt.% Ni-35 wt.% WC and free of iron. This results from the substrate material's dilution effect (AISI 18-2Mn austenitic stainless steel). For the same reason, it is noted that there are significant proportions of Mn and Cr elements, even though the paste was free of them.

It was anticipated that the W content at the bottom of the clad layer would be higher. This is because of the significant density difference between WC (15.63g/cm^3) and Ni (8.9g/cm^3), which causes the WC particles to gravitate towards the bottom of the molten pool. The lower melting point and slower solidification rate of Ni provide time for the WC particles to sink towards the bottom of the molten pool [15]. In contrast, as the W and Ni elements moved from the coating layer's surface to the interface between the clad and substrate, their contents steadily decreased. This may be explained by the dilution effect, which causes the weight percentages of the W and Ni elements to decrease as one approaches the interface and increases the weight percentages of Fe, Mn, and Cr elements. However, higher dilution indicates adequate interfacial bonding with the substrate.

The EDS coloured maps of the C1 clad layer shown in Figure 8 do not exhibit clear variations in the distribution of elements across the different zones of the clad layer. This indicates an almost homogeneous distribution of elements through the clad layer zones.

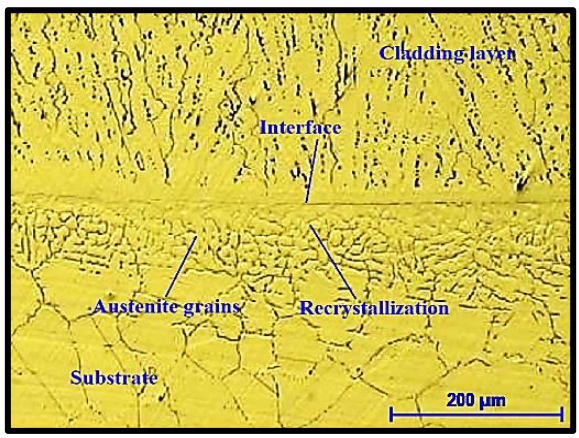

Figure 7. Optical microstructure of the substrate adjacent to the interface of the C1 samp

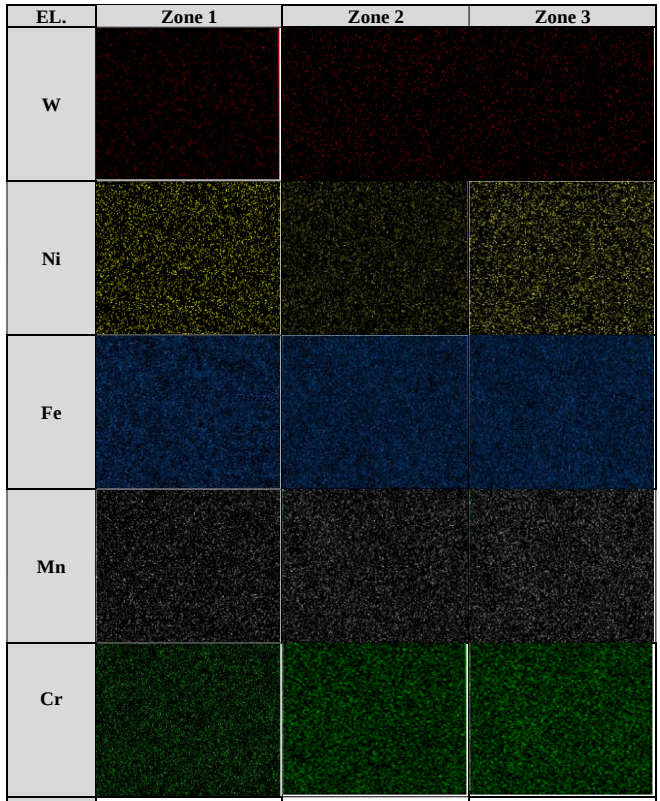

Element	[wt.%]	[wt.%]	[wt.%]
Tungsten	9.00	7.63	7.40
Nickel	13.79	13.39	10.35
Iron	58.30	59.83	61.52
Manganese	8.20	8.44	9.09
Chromium	10.71	10.70	11.64

Figure 8. The EDS map of the C1 sample at different depths along the centerline of the cross section of the clad layer

3.2 The effect of increasing the wt.% of tungsten carbide

Microscopy of the C2 sample resulting from increasing the wt.% of WC to 50% revealed in Figure 9 that the microstructure of Zone 1 of the clad layer consists of insoluble WC particles scattered throughout the matrix of nickel solid solution dendrites. Figure 10 shows the optical and scanning electron microstructures of this zone with higher magnifications, where a decrease in insoluble WC particles was, compared to those that appeared in Zone 1 of the C1 sample (Figure 4) although the increased wt.% of tungsten carbides in the preplaced composite paste, which acts as nuclei for dendrites. Zones 2 and 3 have significantly higher dendritic

densities; the microstructure of these zones, as seen at higher magnifications with the OM and SEM, is depicted in Figures 11 and 12.

Table 6. The EDS elemental composition analysis of the C2 sample at different depths along the centerline of the cross section of the clad layer

Element	Zone 1 [wt.%]	Zone 2 [wt.%]	Zone 3 [wt.%]
Tungsten	3.94	5.84	6.06
Nickel	4.59	4.97	5.92
Iron	68.94	66.72	65.4
Manganese	9.74	9.55	9.69
Chromium	12.79	12.92	12.93

It is clearly noted that the equiaxed and columnar dendrites were less in Zone 2 and Zone 3 of this sample compared to those in the corresponding zones of the C1 sample.

The EDS elemental composition analysis at various depths along the cross sectional centerline of the C2 clad layer is displayed in Table 6 The average content of each element for the three test points was (67.0% Fe, 5.2% Ni, 5.3% W, 9.7% Mn and 12.8% Cr) even though the preplaced composite paste for this sample consisted of 50 wt.% Ni-50 wt.% WC and was free of Fe, Mn and Cr elements. The effect of dilution with the substrate material is to blame for this. But at the expense of the W and Ni contents, the clad layer of this sample had higher Fe, Mn, and Cr contents than the C1 clad layer. This indicates that the substrate material in this sample was diluted more than usual. Furthermore, as the W element moved from the coating layer's surface to the interface between the clad and substrate, its content was observed to have gradually increased. This is because of the significant density difference between WC and Ni, which causes the WC particles to gravitate toward the bottom of the molten pool. This accounts for the observed rise in dendritic density in Zones 2 and 3 (Figures 9, 11 and 12), where the dendritic nuclei are formed by the WC particles.

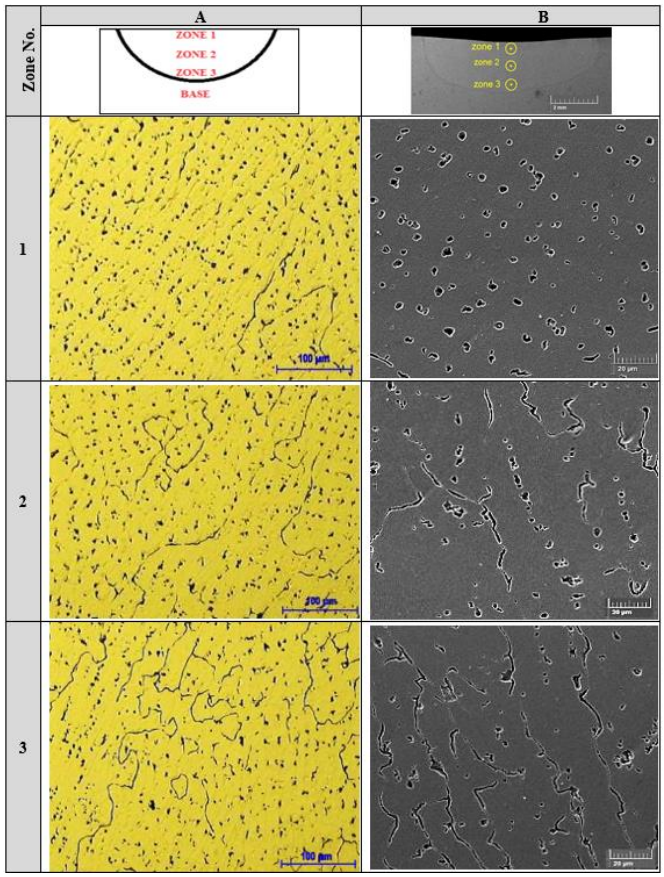

Figure 9. Microstructural map of the C2 sample at different depths along the centerline of the cross section of the clad layer using an (A): OM and (B): SEM

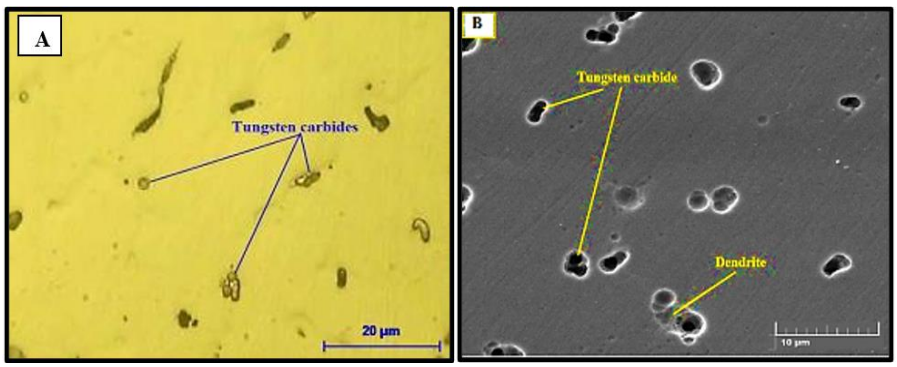

Figure 10. Microstructure of Zone 1 of the C2 sample at higher magnifications using an (A): OM and (B): SEM

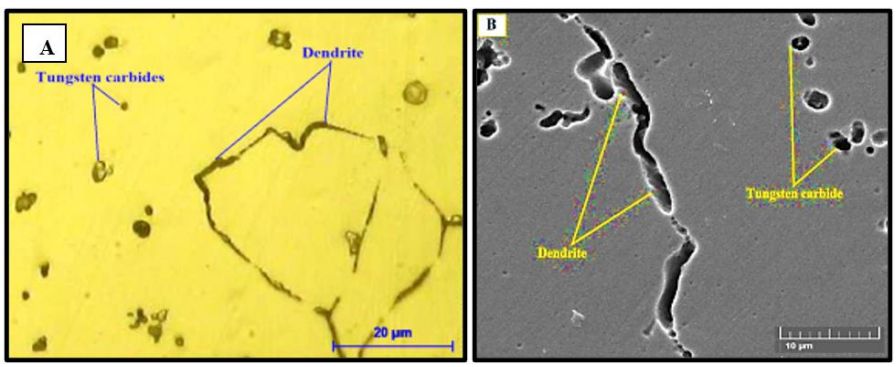

Figure 6. Microstructure of Zone 2 of the C2 sample at higher magnifications usingan (A): OM and (B): SEM.

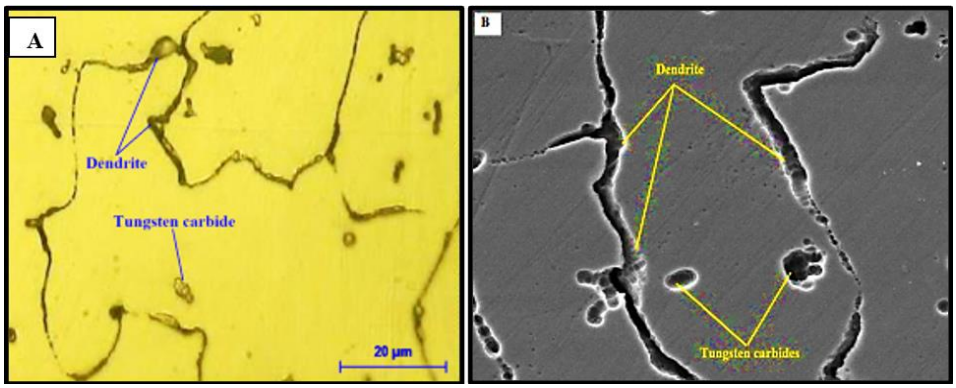

Figure 7. Microstructure of Zone 3 of the C2 sample at higher magnifications usingan (A): OM and (B): SEM

The proportion of dendrites at the various zones along the cross section of the C3 clad layer is greater than that which appeared at the corresponding zones of the C2 sample, as demonstrated by microscopy (Figure 13). This may result from raising the weight percentage of WC in the composite to 65%, which raises the number of dendritic nuclei. Additionally, the SEM showed that columnar grains predominated in Zone 3, whereas equiaxed grains predominated in Zone 1 and a mixture of equiaxed and columnar grains in Zone 2. As one approaches the clad-substrate interface's cooling surface, the percentage of columnar grains rises. The microstructure of the various zones is displayed at higher magnifications in Figure 14.

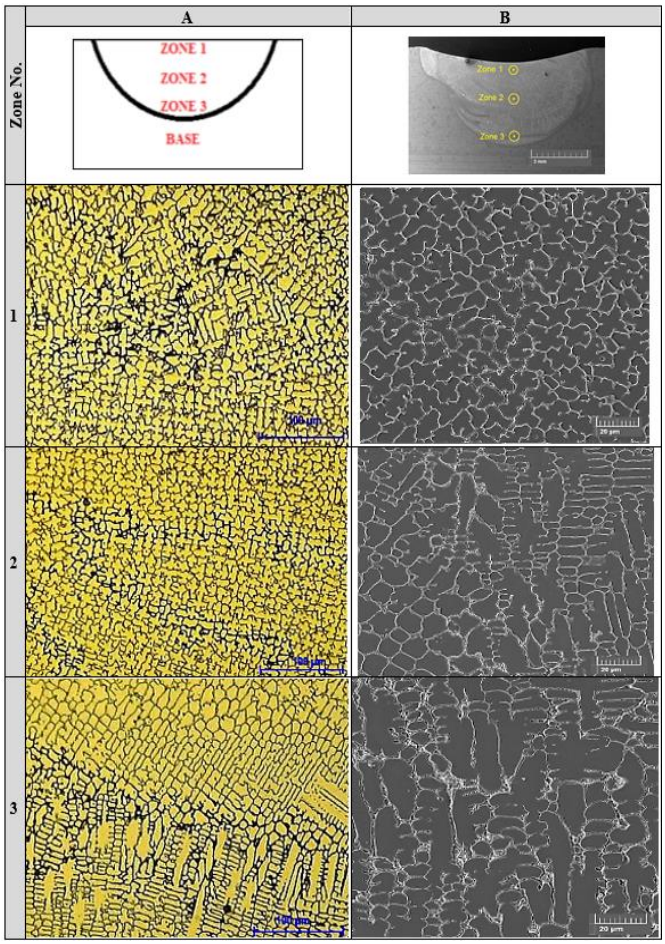

Figure 13. Microstructural map of the C3 sample at different depths along the centerline of the cross section of the clad layer using an (A): OM and (B): SEM

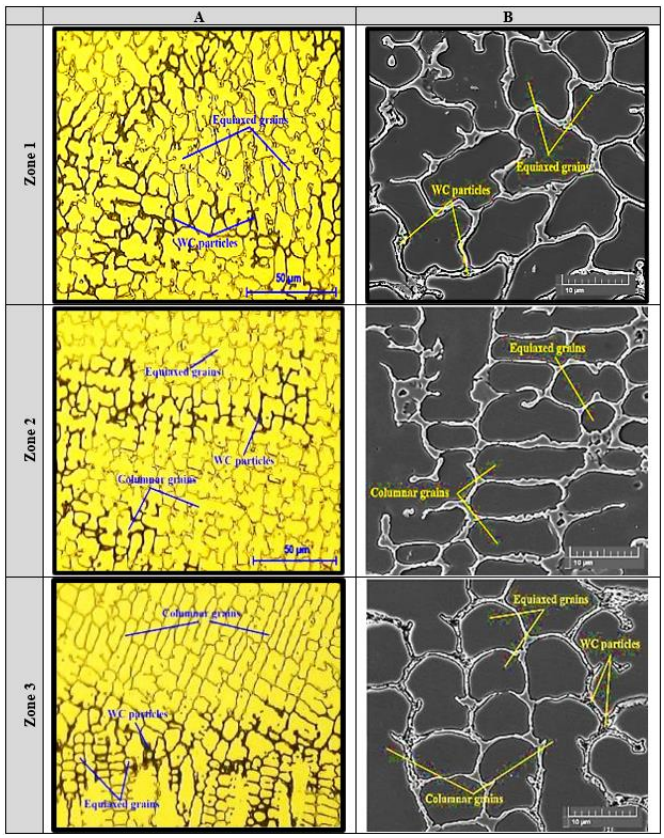

Figure 14. Microstructural map of the C 3 sample at higher magnifications using an (A): OM and (B): SEM

Table 7 shows the average EDS elemental composition along the C3 clad layer's centerline of the cross section: 53.9% Fe, 8.2% Ni, 20.0% W, 7.4% Mn, and 10.5% Cr. It is evident that, in comparison to the C2 layer, the average W content in this clad layer increased significantly. This may be explained by the higher weight percentage of WC in the sample's preplaced composite paste. The higher percentage of dendrites in this sample as opposed to the C2 sample can be explained by this. However, compared to the C2 clad layer, the sample's clad layer had lower average concentrations of Fe, Mn, and Cr. This indicates that there was less dilution of the substrate material in this sample. This could be explained by the fact that a higher TIG cladding current is needed when the weight percentage of WC particles in the preplaced coating layers increases [16]. Therefore, with the use of the same current value of the C2 sample, the dilution will be lower. Lower dilution typically results in an increased proportion of W and Ni in the clad layer.

Table 7. The EDS elemental composition analysis of the C3 sample at different depths along the centerline of the cross section of the clad layer

Element	Zone 1 [wt.%]	Zone 2 [wt.%]	Zone 3 [wt.%]
Tungsten	19.93	21.69	18.3
Nickel	8.55	8.38	7.62
Iron	54.01	52.47	55.36
Manganese	7.06	7.17	7.89
Chromium	10.45	10.3	10.83

The EDS chemical composition analyses of the A and B regions, as shown in the scanning electron microstructure of the C3 sample's Zone 1, are displayed in Figure 15. As the microstructures of A and B regions appear to be heterogeneous, it is evident from the figure that there is a significant difference in the chemical composition analyses of these two regions. Because, as previously indicated, the WC particles act as the dendritic nuclei, the higher W element content at the B region (dendrites) is the result. Conversely, the concentration of Fe and Ni elements is significantly higher at the A region (a Ni-based matrix), suggesting that the iron element is primarily concentrated in the matrix as opposed to the dendritic structure. The Mn weight percentage remained the same, but the Cr weight percentage in the dendritic region was significantly higher than in the matrix.

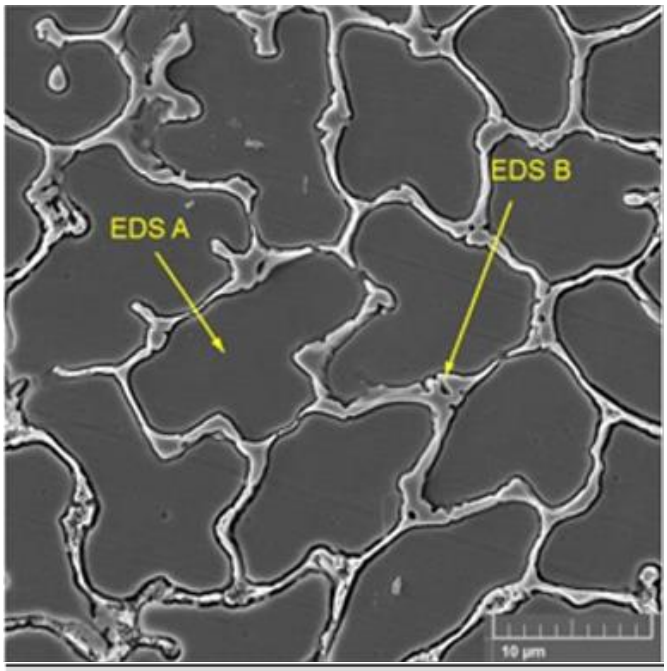

Element	A region [wt.%]	B region [wt.%]
Tungsten	15.29	39.30
Nickel	9.66	2.81
Iron	59.31	34.34
Manganese	6.76	6.56
Chromium	8.98	16.99

Figure 15. EDS elemental composition analysis of A and B regions indicated in the scanning electron microstructure of the Zone 1 of the C3 sample

The proportion of fine dendrites in the three zones depicted in Figure 16 was significantly increased when the weight percentage of WC in the C4 composite was increased to 80% in comparison to the C3 sample. This is attributed to the fact that an increase in the wt.% of WC increases the dendrite nuclei and acts as an obstacle to the growth of dendrites [17, 18]. Therefore, SEM shows that the proportion of dendrites at the different zones is much more than that which appeared at the corresponding zones of the C3 sample. Figure 17 shows the optical and scanning electron microstructures of all three zones at higher magnifications, where it is clearly visible that dendrites are growing at the expense of the matrix. Due to the higher weight percentage of WC in the composite paste—which serves as the nuclei for dendrites—columnar grains predominated in zone 3. Another reason is that the cooling rate at the bottom of the clad layer is faster due to its closer proximity to the cooling surface [15]. This is consistent with what was revealed in 2016 by Shu et al. [19].

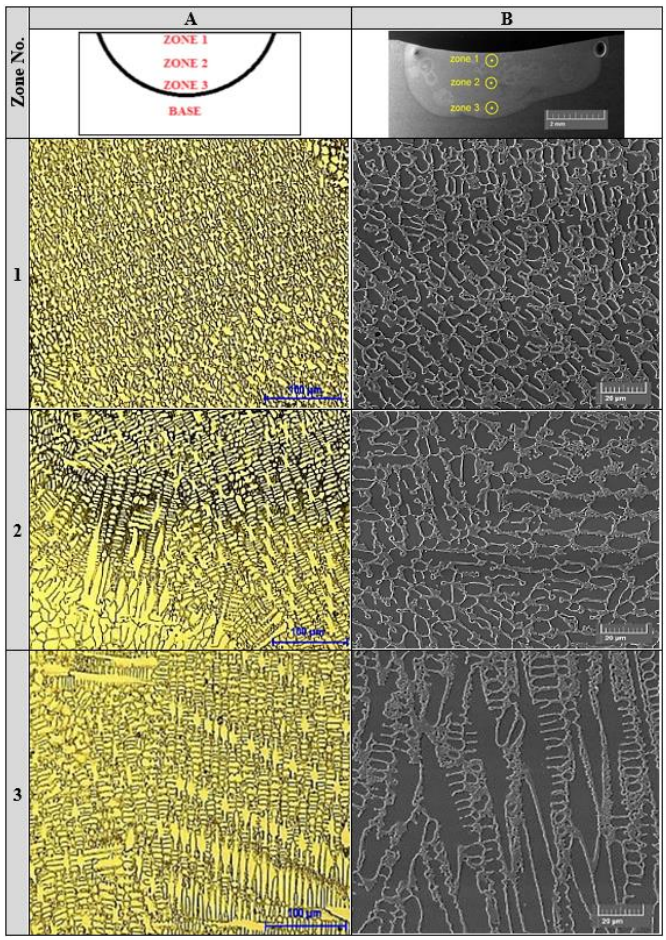

Figure 16. Microstructural map of the C4 sample at different depths along the centerline of the cross section of the clad layer using an (A): OM and (B): SEM

The dark regions appeared in the optical microstructural examination shown in Figures 16 and 17 are actually dendrites with dense branches. This might be due to the effect of increasing the wt.% of WC, which in turn increases the cooling rate. According to Table 8, the average EDS analysis along the C4 clad layer's centerline of cross section was 50.2% Fe, 5.2% Ni, 27.4% W, 7.2% Mn, and 10.0% Cr. The W content of this sample was higher than that of the C3 sample at the expense of the Ni content because the weight percentage of WC in the composite was increased to 80%. As a result, as Figure 17 makes evident, the proportion of dendrites increased at the

expense of the Ni-based matrix. In comparison to the C3 sample, this sample's clad layer has lower concentrations of Fe, Cr, and Mn, indicating less dilution. The decrease in dilution rate might be due to the increased carbide percentage, which results in heat being concentrated on the carbide rather than the substrate. EDS analysis also shows that the variations across the different zones of the C4 clad layer were very minimal indicating an almost homogeneous distribution of elements through the clad layer zones.

Table 8. The EDS chemical composition analysis of the C4 sample at different depths along the centerline of the cross section of the clad layer

Element	Zone 1 [wt.%]	Zone 2 [wt.%]	Zone 3 [wt.%]
Tungsten	28.56	28.7	24.93
Nickel	5.24	5.21	5.05
Iron	49.44	49.04	52.21
Manganese	6.85	7.11	7.54
Chromium	9.91	9.93	10.27

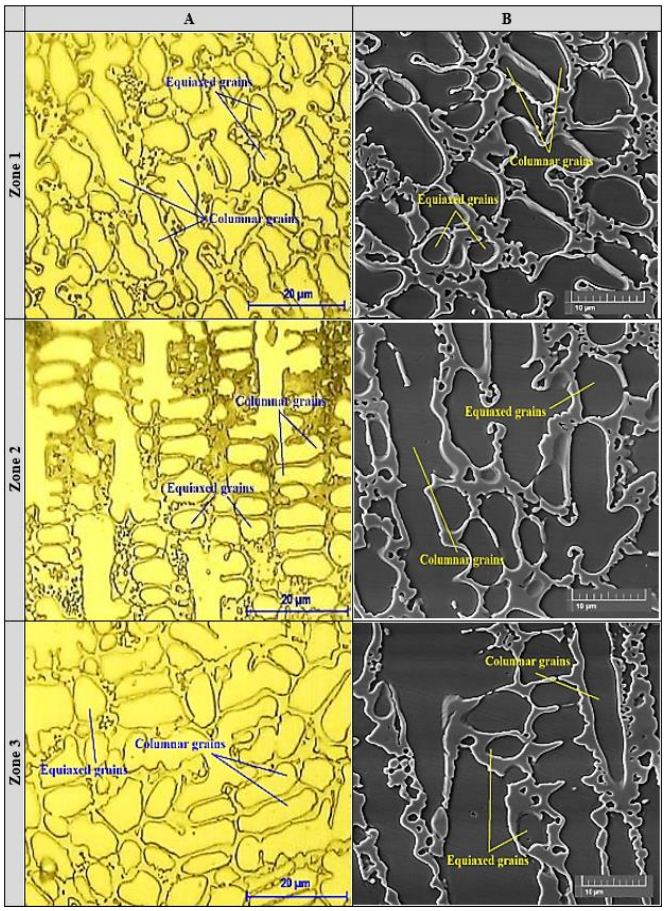

Figure 17. Microstructures of the C 4 sample in the different zones at highermagnifications using an (A): OM and (B): SEM

The increase of the WC weight percentage to 95% at the expense of Ni in the composite layer deposited in the C5 sample led to the formation of a microstructure of dendrites finer than what appeared in the C4 as shown in Figure 18. This is due to the increased percentage of carbides that act as nuclei for dendrites and obstacle their growth. In addition, the optical and scanning electron microstructures showed an increased proportion of columnar dendrites in all three zones. That could be because of the increased cooling rates brought on by a rise in the weight percentage of WC in the composite. Figure 19 shows the optical and scanning electron microstructures of the C5 clad layer with higher magnifications. Table 9 presents the results of an EDS analysis conducted along the centerline of the cross section of the C5 clad layer. The average chemical composition of this layer was 54.9% Fe, 1.1% Ni, 25.1% W, 7.8% Mn, and 11.1% Cr.

It is readily apparent that the W content is substantially higher than Ni when the weight percentage of WC in the sample composite is increased to 95%. It is also noted that the average weight percentage of iron is relatively high at the expense of the other elements. The average wt.% of Fe in the previous five samples was however not less than 50%. This indicates a greater dilution and higher participation of iron in the matrix, resulting in good bonding with the substrate.

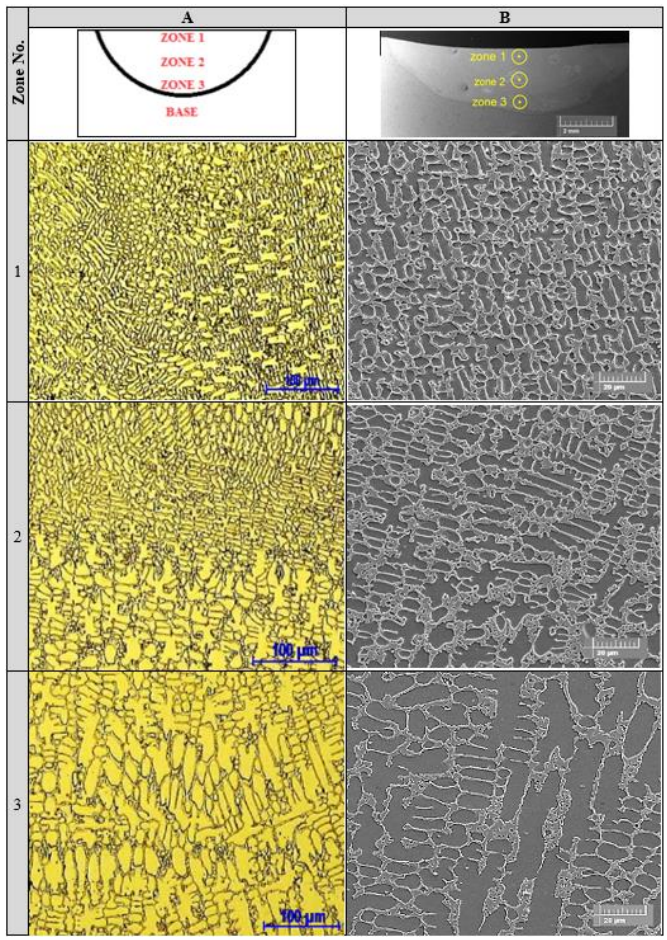

Figure 18. Microstructural map of the C5 sample at different depths along thecenterline of the cross section of the clad layer using an (A): OM and (B): SEM

Table 9. The EDS chemical composition analysis of the C5 sample at different depths along the centerline of the cross section of the clad layer

Element	Zone 1 [wt.%]	Zone 2 [wt.%]	Zone 3 [wt.%]
Tungsten	25.71	27.33	22.42
Nickel	0.99	1.15	1.12
Iron	53.94	53.4	57.24
Manganese	7.79	7.43	8.05
Chromium	11.56	10.7	11.16

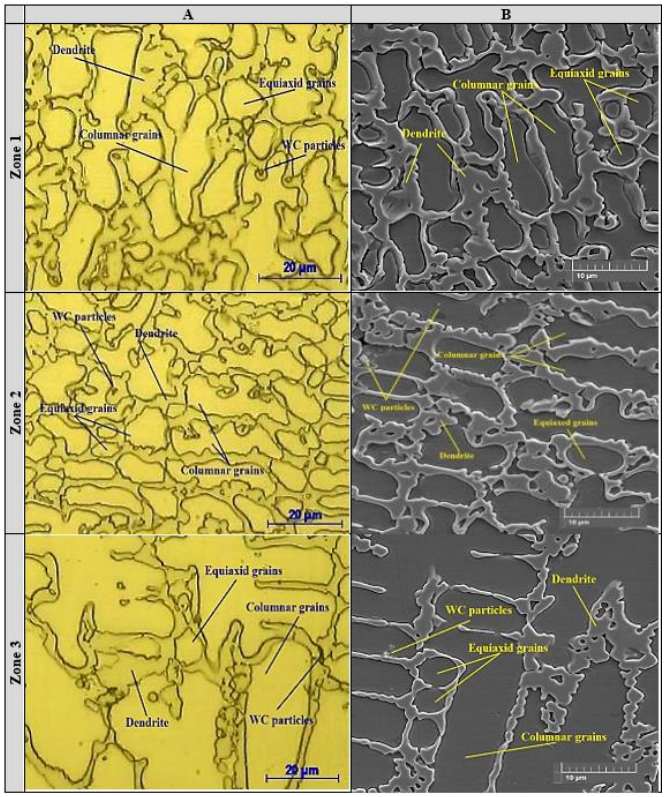

Figure 19. Microstructures of the C5 sample in the different zones at higher magnifications using an (A): OM and (B): SEM

4. CONCLUSION

This study explored the effect of using different wt.% of WC (35, 50, 65, 80, and 95) on WC-Ni composite coatings deposited on AISI 18-2Mn austenitic stainless steel substrates using the TIG cladding technique at a travel speed of 67 mm/min. and a current value of 130A. The most important results of this study can be concluded as follows:

1. The microstructure of the substrate material was austenite grains noting the appearance of twinning.
2. The wt.% of WC had a significant effect on the microstructures across the coating layers.
3. The microstructures of the C1 sample clad layer (35% WC-Ni and 130A) and a travel speed of 67 mm/min. were mainly composed of nickel solid solution dendrites with insoluble intermetallic compounds of WC particles distributed through an austenitic matrix.
4. The bottom regions showed the columnar grains were the predominant at the clad-substrate interface.
5. Increasing the wt.% of WC to 50% at the same current and travel speed value (C2 sample) notably decreased insoluble WC particles, compared to those that appeared in Zone 1 of the C1 sample, which, somewhat, increased the density of dendrites while moving towards the bottom of the coating layer.
6. The microstructures of the C3 sample (65 wt.% of WC) were notably finer, and the proportion of dendrites was much higher. The proportion of columnar grains increases while approaching the cooling surface of the clad-substrate interface.
7. With C4 sample (60 wt.% of WC), the proportion of dendrites and carbides clearly increased at the expense of the matrix. The dendrites were also more densely branched.
8. Increasing the wt.% of WC to 95% led to the formation of finer and mostly columnar dendrites across the C5 clad layer.

5. RECOMMENDATIONS

The lessons learned from this study can be taken into account in studies related to cladding, and some areas covered in this study could be further improved. The following is a summary of recommendations for further work.

1. Corrosion testing for the coating layers can be carried out.
2. Laser cladding technique can be used with the clad layer compositions used in this study.
3. Studying the effect of current value on the microstructure and properties of the clad layers.
4. Investigating the influence of particle size of pre-placed composite powders on the characteristics of the clad layers.
5. Cladding other substrate materials such as tool steels, nickel alloys, aluminum alloys and magnesium alloys.

REFERENCES

[1] Lo, K.H., Shek, C.H., Lai, J.K.L. (2009). Recent developments in stainless steels. Materials Science and Engineering: R: Reports, 65(4-6): 39-104. https://doi.org/10.1016/j.mser.2009.03.001

[2] Baddoo, N.R. (2008). Stainless steel in construction: A review of research, applications, challenges and opportunities. Journal of Constructional steel Research, 64(11): 1199-1206. https://doi.org/10.1016/j.jcsr.2008.07.011

[3] Rossi, B. (2014). Discussion on the use of stainless steel in constructions in view of sustainability. Thin-Walled Structures, 83: 182-189. https://doi.org/10.1016/j.tws.2014.01.021

[4] Davis, J.R. (1994). Stainless Steels. New York: ASM.

[5] Rius-Ayra, O., Llorca-Isern, N. (2021). Special Issue "Surface modification of metals and alloys". Coatings, 11(2): 260. https://doi.org/10.3390/coatings11020260

[6] Bose, S., Robertson, S.F., Bandyopadhyay, A. (2018). Surface modification of biomaterials and biomedical devices using additive manufacturing. Acta Biomaterialia, 66: 6-22. https://doi.org/10.1016/j.actbio.2017.11.003

[7] Nouri, A., Wen, C. (2015). Introduction to surface coating and modification for metallic biomaterials. Surface Coating and Modification of Metallic Biomaterials, 3-60. https://doi.org/10.1016/B978-1-78242-303-4.00001-6

[8] Kireeva, I.V., Luzginova, N.V., Chumlyakov, Y.I., Karaman, I., Lichter, B.D. (2004). Plastic deformation of nitrogen-containing austenitic stainless steel single crystals with low stacking fault energy. Journal de Physique IV, 115: 223-230. https://doi.org/10.1051/jp4:2004115027

[9] Nouri, A., Wen, C. (2021). Stainless steels in orthopedics. In Structural Biomaterials. Woodhead Publishing, pp. 67-101 https://doi.org/10.1016/B978-0-12-818831-6.00008-2

[10] Phillips, D.H. (2023). Welding Engineering: An Introduction. John Wiley & Sons.
[11] Sheets, A.S.G.D. (2013). Atlas steels technical handbook of stainless steels. Stainless Steel, 630: 17-4PH. https://atlassteels.com.au/wp-content/uploads/2021/08/Atlas-Steels-Technical-Handbook-of-Stainless-Steels-12-08-21.pdf.
[12] Maistro, G. (2015). Microstructural Characterization of Expanded Austenite in 304L and 904L Austenitic Stainless Steels. Chalmers Tekniska Hogskola (Sweden).
[13] Zhang, D., Zhang, X. (2005). Laser cladding of stainless steel with Ni–Cr_3C_2 and Ni–WC for improving erosive–corrosive wear performance. Surface and Coatings Technology, 190(2-3): 212-217. https://doi.org/10.1016/j.surfcoat.2004.03.018
[14] Yin, H., Song, W., Liu, Q., Zhu, G., Zhang, J., Yu, Y., Yin, C. (2022). Effect of different contents of WC on microstructure and properties of NiCrMo coatings prepared by PTA. Coatings, 12(10): 1574. https://doi.org/10.3390/coatings12101574
[15] Tosun, G. (2014). Ni–WC coating on AISI 1010 steel using TIG: Microstructure and microhardness. Arabian Journal for Science and Engineering, 39: 2097-2106. https://doi.org/10.1007/s13369-013-0754-3
[16] Pawlowski, L. (1999). Thick laser coatings: A review. Journal of Thermal Spray Technology, 8: 279-295. https://doi.org/10.1361/105996399770350502
[17] Tijo, D., Masanta, M., Das, A.K. (2018). In-situ TiC-TiB_2 coating on Ti-6Al-4V alloy by tungsten inert gas (TIG) cladding method: Part-I. Microstructure evolution. Surface and Coatings Technology, 344: 541-552. https://doi.org/10.1016/j.surfcoat.2018.03.082
[18] Pawlowski, L. (1999). Thick laser coatings: A review. Journal of Thermal Spray Technology, 8: 279-295. https://doi.org/10.1361/105996399770350502
[19] Shu, D., Li, Z., Zhang, K., Yao, C., Li, D., Yuan, Y., Dai, Z. (2017). Phase constituents and growth mechanism of laser in situ synthesized WC reinforced composite coating with W–C–Ni system. Journal of Materials Research, 32(3): 557-565. https://doi.org/10.1557/jmr.2016.469